RESEARCH ARTICLE

POLYMER ENGINEERING AND SCIENCE WILEY

Molecular mobility in high-performance polynorbornenes: A combined broadband dielectric, advanced calorimetry, and neutron scattering investigation*

Mohamed A. Kolmangadi[1] | Paulina Szymoniak[1] | Reiner Zorn[2] |
Martin Böhning[1] | Marcell Wolf[3] | Michaela Zamponi[4] | Andreas Schönhals[1]

[1]Bundesanstalt für Materialforschung und -prüfung (BAM), Berlin, Germany

[2]Forschungszentrum Jülich GmbH, Jülich Centre for Neutron Science (JCNS-1) and Institute for Biological Information Processing (IBI-8), Jülich, Germany

[3]Heinz Maier-Leibnitz Zentrum (MLZ), Technische Universität München, Garching, Germany

[4]Forschungszentrum Jülich GmbH, Jülich Centre for Neutron Science at MLZ, Garching, Germany

Correspondence
Reiner Zorn, Forschungszentrum Jülich GmbH, Jülich Centre for Neutron Science (JCNS-1) and Institute for Biological Information Processing (IBI-8), 52425 Jülich, Germany.
Email: r.zorn@fz-juelich.de

Andreas Schönhals, Bundesanstalt für Materialforschung und -prüfung (BAM), Unter den Eichen 87, 12205 Berlin, Germany.
Email: andreas.schoenhals@bam.de

*Gregory B. McKenna Virtual Issue

Abstract

The molecular dynamics of two addition type polynorbornenes, exo-PNBSi and PTCNSi1, bearing microporosity has been investigated by broadband dielectric spectroscopy, fast scanning calorimetry, and neutron scattering. Both polymers have the same side groups but different backbones. Due to their favorable transport properties, these polymers have potential applications in separation membranes for gases. It is established in literature that molecular fluctuations are important for the diffusion of small molecules through polymers. For exo-PNBSi, two dielectric processes are observed, which are assigned to Maxwell/Wagner/Sillars (MWS) process due to blocking of charge carriers at internal voids or pore walls. For PTCNSi1, one MWS-polarization process is found. This points to a bimodal pore-size distribution for exo-PNBSi. A glass transition for exo-PNBSi and for PTCNSi1 could be evidenced for the first time using fast scanning calorimetry. For T_g and the corresponding apparent activation energy, higher values were found for PTCNSi1 compared to exo-PNBSi. For both polymers, the neutron scattering data reveal one relaxation process. This process is mainly assigned to methyl group rotation probably overlayed by carbon–carbon torsional fluctuations.

KEYWORDS

advanced calorimetry, dielectric spectroscopy, neutron scattering, polynorbornenes

1 | INTRODUCTION

Key technologies in many industries are separation processes, which also contribute massively to the global energy consumption. Compared to conventional techniques, which are based on cryogenic, or adsorption routes, membrane processes are essentially more energy and cost efficient. Also, membrane-based approaches for gas and hydrocarbon separations are essential constituents for a greener way in sustainable energy supply, in renewable biogenic processes (biogas upgrading) as well as in treatment of fossil natural gas. The most interesting candidates for the active layer in separation membranes are glassy polymers. Polymers are relatively cheap in comparison to other materials and moreover they can be easily processed into membranes on larger scales.

The widely accepted model to describe the transport of gas molecules in the free volume of dense (i.e., nonporous) polymers is the solution-diffusion model.[1,2] It is based on the assumptions that a gas molecule is sorbed at a membrane surface (described by the solubility S) and then diffuses through the membrane (described by the diffusion coefficient D) across a concentration gradient as driving force, being finally desorbed at the opposite surface. The polarizability controls mainly the solubility of a gas molecule in the polymeric membrane, whereas the diffusivity is related its effective size. The latter can be described by the minimal diameter of the molecule enabling its diffusion through bottlenecks of the polymeric matrix, which can be static or dynamic in nature. In conventional polymers employed in gas separation membranes like, for instance, high-performance polyimides, the diffusion of a gas molecule in the free volume of the polymer is related to the molecular mobility of the matrix and thus an activated process.[3,4]

There are two key parameters to quantify the efficiency of polymers for gas separation membranes. The first performance parameter is the permeability P which is given in the solution-diffusion model by the product $P = D * S$. Roughly spoken, P corresponds to the flux of gas molecules through the membrane. Therefore, P should be high. The second important quantity for gas separation membranes is the permselectivity $\alpha_{a,b}$ which is defined as ratio of the permeabilities of two different gasses a and b $\alpha_{a,b} = P_a/P_b$, representing the ability for separation. To have an effective separation process, also the permselectivity should be high. However, there is a well-known trade-off relationship between the permeability and the permselectivity: when P increases, $\alpha_{a,b}$ decreases. This trade-off is characterized by the so-called Robeson-upper-bound.[5–63]

According to the solution-diffusion approach, glassy polymers with a high free volume are the most attractive materials for the active separation layer in membranes.[8] For that reason, attempts have been made to obtain polymers with a high free volume. This process leads to the synthesis of polyacetylene derivatives like poly (trimethylsilylpropyne) (PTMSP)[9] and poly(4-methyl-2-pentyne) (PMP).[10,11] These two polymers and other polyacetylenes[12] have still the highest permeability values reported in literature up to now, but they are also characterized by poor permselectivities. A different performance behavior, characterized by high permeability values and sufficient permselectivities, is observed for more recently developed groups of polymers, which are characterized by an extremely high free volume like polymers of intrinsic microporosity (PIMs)[13,14] or addition-polymerized poly(norbornenes) or poly(tricyclononenes)[15–19] with Si-substituted bulky side groups. Like PIMs, the

mentioned poly(norbornenes) bear also microporosity, which results from a rigid backbone and the bulky side group substituents. Especially the latter structural units prevent an effective packing of segments in the condensed state leading to Brunauer/Emmett/Teller (BET) surface areas of several hundred m^2/g.[18,19] A comparison of BET surface areas of microporous polynorbornenes and PIMs can be found in the literature.[20,21] The observed pore sizes are found to be between 0.5 nm and 2 nm, that is, micropores according to IUPAC classification.

The pores in these polymers bearing intrinsic microporosity form an interconnected network of micropores, which was also evidenced by molecular dynamic simulations.[22,23] For this interconnected pore network, a more Knudsen-like diffusion is expected rather than a thermally activated and size-discriminating sieving process, which leads to the observed reasonable permselectivity values. It is discussed in the literature that a change from Knudsen diffusion and solution-diffusion takes place in the pore size range of 0.5–1 nm.[1,5] This transition is significantly influenced by the temporal stability of the pore network as well as by the size of a diffusing gas molecule. Considering the enthalpic and entropic contributions to the selectivity of the diffusion, Koros and Zhang established a classification between (a) molecular sieves, which are completely rigid, (b) semi-rigid polymers, and (c) flexible polymers.[24] Microporous poly(norbornenes) and other polymers bearing microporosity like PTMSP and PIMs belong to the class of semi-rigid polymers for which a combination of both diffusion mechanisms is assumed. This combination is confirmed by an observed deviation from the usually found linear dependence of the diffusion coefficient on the squared minimal diameter of the gas molecule.[25] This seems to indicate a difference in transport mechanism for small gas molecules and larger ones. In other words, small molecules like H_2 or He exhibit a more Knudsen-like diffusion through the interconnected pore network, whereas molecules with a larger effective diameter like O_2, CO_2, N_2, or CH_4 follow a stronger size discriminating solution-diffusion mechanism, which is thermally activated. This means that the small penetrants see an unchanging rigid pore network, but larger molecules see temporary channels in a fluctuating matrix. In that respect, it remains an open question whether the solution-diffusion transport mechanism is due to molecular fluctuations in the backbone or the side groups of the polymer, which can dynamically enlarge bottleneck windows between pores at a time scale relevant for gas transport. Such an approach to the permselectivity of polyacetylene derivatives was discussed by Kanaya et al. in the frame of a random gate model.[26] Therefore, it is important to investigate and to
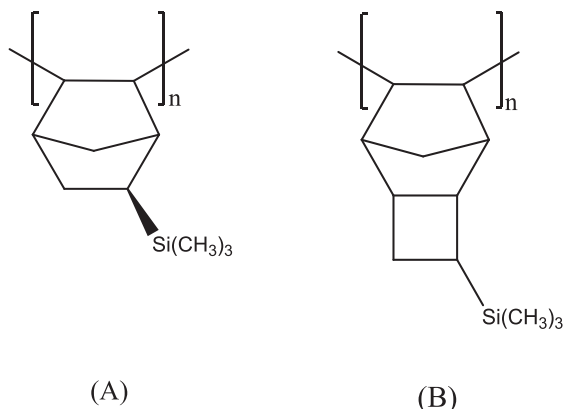
FIGURE 1 Chemical structure of exo-PNBSi (A) and PTCNSi1 (B). Note that for exo-PNBSi, stereochemical orientation of the trimethyl silyl side group is fixed, whereas for PTCNSi1, the orientation of the trimethyl silyl side group is random

understand the molecular dynamics of such microporous polymers further.

Here, the molecular mobility of two addition-polymerized polynorbornenes is investigated and compared by a combination of broadband dielectric spectroscopy, advanced calorimetry, and neutron scattering. The discussed poly(norbornenes) have the same Si-substituted side group but different backbone structures. It should be noted that the influence of the polymerization mechanism (addition or metathesis) on the molecular mobility was discussed recently.[27]

2 | MATERIALS AND METHODS

2.1 | Materials

The first investigated polymer is a poly(norbornene) with a trimethylsilyl side group denoted as exo-PNBSi. Its chemical structure is given in Figure 1A. Its synthesis is described elsewhere.[28] The molecular weight of the polymer is $M_w = 1.6 \times 10^6$ g mol^{-1}. The BET surface area of exo-PNBSI was estimated to 540 m^2 g^{-1}. No glass transition could be found for exo-PNBSi by conventional differential scanning calorimetry (DSC) before the thermal degradation of the polymer, but it was speculated in the literature[29] from mechanical measurements that it should be located at temperatures between 293 and 303°C (566 and 576 K). The low-frequency vibrational density of states of exo-PNBSi estimated by inelastic neutron scattering is discussed in the literature.[20]

The data obtained for exo-PNBSi will be compared with results for a polytricyclononene called PTCNSi1 where its structure is given in Figure 1B. The synthesis of PTCNSi1 is described in the literature.[17] The molecular

weight M_w is 5.5×10^5 g mol^{-1} and the BET surface area is estimated to 610 m^2 g^{-1}.[16] Like for exo-PTNBSi, no glass transition could be found by conventional DSC. A dielectric investigation of PTCNSi1 is reported in the literature.[30] More recently, the molecular dynamics of PTCNSi1 on microscopic length and times scales was investigated by quasielastic neutron scattering,[31] where its low-frequency density of states was evaluated by inelastic neutron scattering.[20] The data for PTCNSi1 will be taken from these references.

Due to the cyclobutane ring, the backbone rigidity should be higher for PTCNSi1 compared to exo-PNBSi. This was confirmed by hydrodynamic and electrooptical measurements.[32] The Kuhn segment length was estimated to 4.7 nm for the same exo-PNBSi but with an irregular substitution and 6 nm for PTCNSi1, which also indicates a higher chain rigidity for the latter polymer. Nevertheless, both materials belong to the group of semi-rigid polymers because the Kuhn segment length is below 10 nm.[33]

The preparation of the samples for the measurements is described in detail elsewhere.[30] In short, exo-PNBSi was dissolved in toluene. The concentration of the solution, mainly affecting the obtained film thickness, was adapted to the requirements of the different experimental methods. For the dielectric measurements, films with a thickness of ca. 60 μm were prepared, whereas for the neutron scattering experiments, the samples had a thickness of ca. 130 μm, which corresponds to a ca. 10% incoherent neutron scatterer to minimize multiple scattering events.

The solution was cast in a Teflon mold after filtration through a 0.2 μm PVDF filter. Then the mold was located in a closed chamber saturated with toluene vapor to slow down the evaporation rate. After approximately 3 days, a solid film was obtained. The film was placed in an oven with oil-free vacuum at a temperature of 393 K (120°C) for 3 days to completely remove residual solvent from the sample.

2.2 | Methods

2.2.1 | Dielectric spectroscopy

The complex permittivity or dielectric function $\varepsilon^*(f) = \varepsilon'(f)-i\varepsilon''(f)$ was measured with a high-resolution Alpha analyzer (Novocontrol, Montabaur). Here, ε' and ε'' are the real and the imaginary parts of the complex permittivity, f denotes the frequency (radial frequency $\omega = 2\pi f$), and i is the imaginary unit. The Alpha analyzer was interfaced to a sample holder with an active head. The data were measured isothermally in the frequency

range from 10^{-1} Hz to 10^6 Hz in a broad temperature range. To establish a good electrical contact of the electrodes with the sample Al-electrodes with a diameter of 10 mm were evaporated to the surface of the sample in high vacuum. The temperature of the sample was controlled by a Quatro temperature controller, which operates with a heated nitrogen stream. The temperature has a stability better than 0.1 K. For details, the reader is referred to the literature.[34] The measurements were carried out in the following cycles: First heating, first cooling, and second heating.

2.2.2 | Fast scanning calorimetry

To investigate the thermal behavior, and especially the glass transition, fast scanning calorimetry (FSC) is employed by utilizing a Mettler Toledo Flash DSC 1. It is based on MultiSTAR UFS 1 twin chip sensors as sample cells. Due to the microsized chip and the low masses of the samples, it enables calorimetric measurements with a heating rate ranging from 0.5 to 10^4 K s^{-1}.[35] The available cooling rates are approximately one order of magnitude lower. The measurements were carried out in a symmetric way this means employing the same cooling and heating rate. The base temperature of the Flash DSC 1 was controlled by a TC100 intracooler from Huber. To establish a good thermal contact between the sample and the sensor and to reduce the thermal lag, a high viscosity silicon oil of the type AK 60000[36] (Wacker Chemie AG) is used. Standardized procedures recommended by the instrument manufacturer have been applied for the conditioning and the calibration of the sensor. Nitrogen was used as purge gas at a flow rate of 40 ml min^{-1}.

It was proven that FSC enables to decouple the kinetics of degradation from other effects like melting,[37,38] the glass transition,[39–41] or the chain dynamics.[42,43]

2.2.3 | Neutron scattering

Quasielastic neutron scattering senses molecular fluctuations at microscopic length and time scales.[44] During the scattering process, momentum and energy are exchanged between the neutron and a nucleus. As main experimental information the double differential cross section $d^2\sigma/d\Omega\,d\omega$ is extracted from the scattered data. It is defined by

$$\frac{d^2\sigma}{d\Omega\,d\omega} = \frac{1}{4\pi}\frac{k_f}{k_i}\left(\sigma_{\mathrm{coh}}S_{\mathrm{coh}}(q,\omega) + \sigma_{\mathrm{inc}}S_{\mathrm{inc}}(q,\omega)\right) \quad (1)$$

In Equation (1), k_i and k_f are the incident and final wave vectors of the neutron beam. Their differences define the scattering vector $q = k_f - k_i$ where Ω is the solid angle of detection. The measured energy transfer ΔE is related to the angular frequency by $\omega = \Delta E/\hbar$. The coherent ($i = \mathrm{coh}$) and incoherent ($i = \mathrm{inc}$) scattering functions (dynamic structure factors) are denoted by $S_i(q,\omega)$. The coherent and incoherent scattering is weighted by corresponding scattering cross-section σ_i. The polymer exo-PNBSi contains silicon (Si), carbon (C), and hydrogen (H) nuclei. From its chemical structure, $\sigma_{\mathrm{coh}} = 89.3$ barn and $\sigma_{\mathrm{inc}} = 1444.7$ barn are deduced. This means that the measured scattering is mostly incoherent. The same is true for PTCNSi1.[31]

Different spectrometers were employed for the neutron scattering experiments. All measurements were carried out at the Heinz-Maier-Leibnitz Zentrum (MLZ) at Garching, Germany. An overview about the molecular dynamics at a time of approximately 2 ns can be deduced by fixed elastic window scans ($\Delta E \approx 0$) utilizing a neutron backscattering spectrometer. The measurements were carried out utilizing the high-resolution backscattering instrument SPHERES.[45,46] SPHERES is a cold neutron backscattering spectrometer of the third generation operated by Jülich Centre for Neutron Science (JCNS) at the MLZ. Besides a focusing neutron optics, it is equipped with a rotating phase-space-transform chopper and a linear Doppler drive. The incident wavelength of $\lambda_n = 6.27$ Å together with a standard configuration gives a maximal accessible elastic scattering vector of $q = 1.76$ Å^{-1}. An effective mean-squared displacement $\langle u^2 \rangle_{\mathrm{eff}}$ is calculated by fitting the expression

$$\frac{I_{el}(q)}{I_0(q)} = \exp\left(-\frac{\langle u^2 \rangle_{\mathrm{eff}} q^2/3}{1 + \alpha_2 \langle u^2 \rangle_{\mathrm{eff}} q^2/6}\right) \quad (2)$$

to the data with a term representing multiple scattering added. α_2 is an effective non-Gaussianity parameter. The function in the argument of the exponential was chosen to have the standard terms of a cumulate expansion up to q^4 but not that value of the exponential becomes greater than one in the limit $q \to \infty$ as a simple truncation of the series would give. Compared to the Gaussian standard approach, this function is more reliable when $\langle u^2 \rangle_{\mathrm{eff}}$ becomes large, but it does not assume a specific model as in the literature.[47] $I_{el}(q)$ and $I_0(q)$ are the elastically and totally scattered intensities. $I_0(q)$ is obtained by a measurement with an increased statistic at 4 K. The scans were measured with a heating rate of 0.98 K min^{-1} (0.245 K per data point).

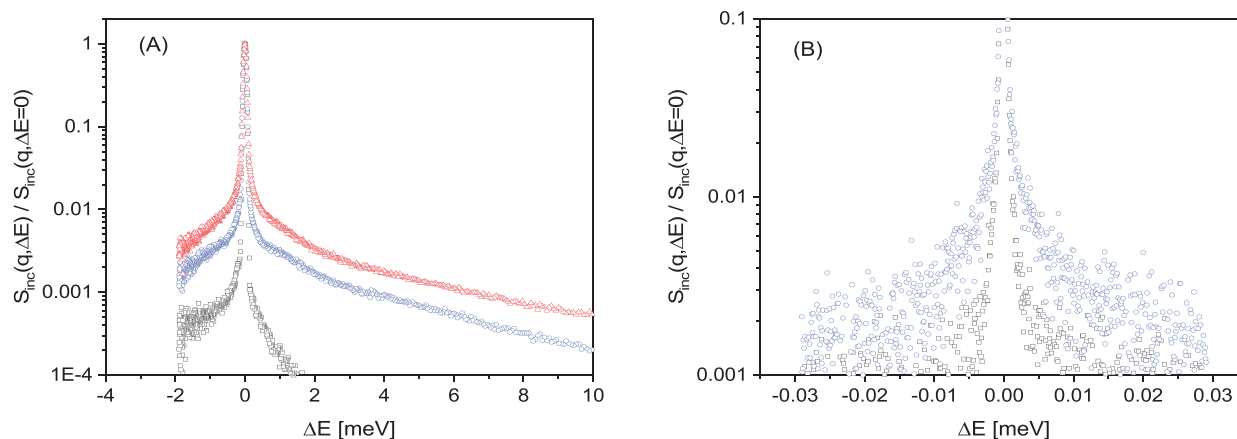The quasielastic measurements were carried out by a combination of neutron time-of-flight (TOF) spectroscopy

FIGURE 2   (A) Incoherent dynamical structure factor $S_{Inc}(q,\Delta E)$ normalized by the height of the elastic line measured for exo-PBNSi at TOFTOF at an angle of 91.3°: black squares—resolution (4 K); blue circles—125 K, red triangles—200 K. (B) Incoherent dynamical structure factor $S_{Inc}(q,\Delta E)$ normalized by the height of the elastic line measured for exo-PBNSi at SPHERES at an angle of 90°: black squares—resolution (4 K); blue circles—125 K

and neutron backscattering (BS). For the TOF experiments, the cold neutron time-of-flight spectrometer TOFTOF is utilized, which is operated at the MLZ by the Technische Universität München.[48] A standard configuration with an incident wave length of $\lambda_n = 5.0$ Å gives a resolution from 77 to 99 µeV (full width at half maximum [FWHM], increasing with higher scattering angles) where the highest elastic scattering vector is $q = 2.3$ Å^{-1}. The high-resolution spectrometer SPHERES (see above) is employed for the quasielastic backscattering measurements. Like for the elastic scans, it was used with an incident wavelength of $\lambda_n = 6.27$ Å in standard configuration. The average resolution was 0.65 µeV at FWHM. A measurement of the sample at 4 K provides the resolution of both instruments by assuming that besides quantum-mechanical zero-point motions all molecular fluctuations and vibrations are frozen. For the evaluation of the TOF measurements, the program INX was used for the whole process of data reduction, corrections, TOF to energy transformation as well as for a normalization to a vanadium standard and background. subtraction.[49] For the evaluation of the backscattering data, the software SQW was used that applies backscattering and vanadium normalization, self-attenuation correction as well as a self-attenuation correction to the background data, which must be subtracted from the data.[50] Effective but cross-sectional weighted incoherent dynamic scattering functions were calculated by both programs in dependence of q and ΔE. Figure 2 depicts the incoherent dynamic structure factors measured for exo-PNBSi at TOFTOF (Figure 2A) and SPHERES (Figure 2B). Both types of spectra show the quasielastic broadening indicating molecular motions. The data measured by TOFTOF and SPHERES have a large difference in their energy

resolution. To analyze both data sets together, they were Fourier transformed and divided by the Fourier transform of the corresponding resolution. By this procedure, absolute values of the incoherent intermediate scattering function in time domain $S_{inc}(q,t)$ were obtained. Moreover, a correction scheme working in time domain was employed to correct the data for multiple scattering events because the exact scattering required for a Monte Carlo determination is not known.[51] The method is based on the idea to develop the scattering into a series of multiple scattering fractions and to optimize these according the theoretical limit of $S_{inc}(q,t) = 1$ for $q \rightarrow 0$. The multiple scattering fractions for exo-PNBSi were found to be 21% for both instruments. The multiple scattering fractions estimated for PTCNSi1 can be found in the literature.[31]

3 | RESULTS AND DISCUSSION

3.1 | Broadband dielectric spectroscopy

Figure 3A depicts the dielectric loss of exo-PNBSi versus frequency and temperature in a 3D representation. The dielectric spectrum shows different dielectrically active processes. At lowest temperatures (or highest frequencies), a so-called β_1*-process is observed. This process is followed by a β_2*-process at higher temperatures or lower frequencies. A conductivity contribution due to the drift motion of charge carriers is observed for the highest temperatures.

The dielectric behavior of PTCNSi1 is already discussed in the literature.[30] At low temperatures, a β-relaxation is observed. Because PTCNSi1 and exo-PNBSi
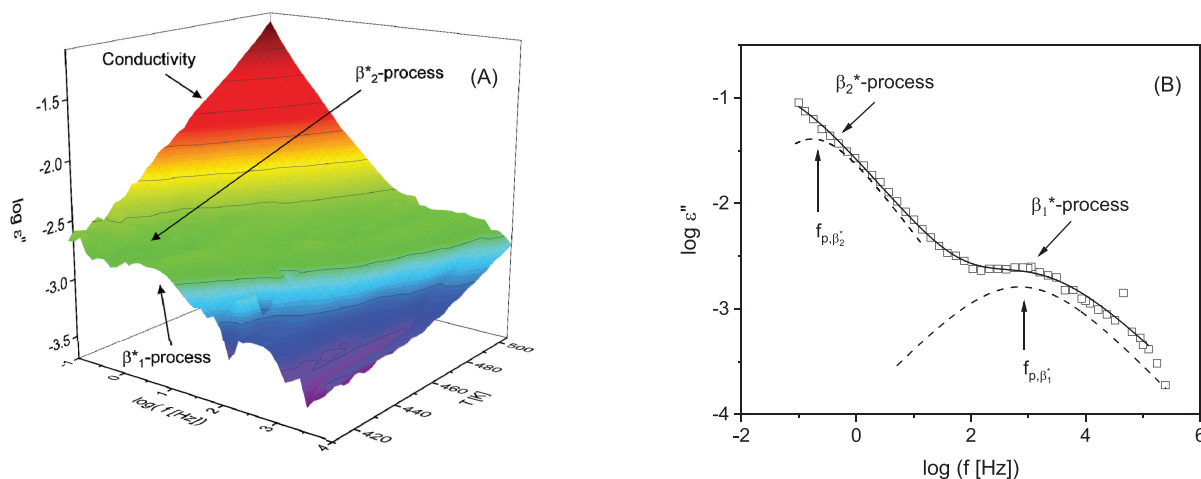
FIGURE 3 (A) Dielectric loss versus frequency and temperature for exo-PNBSi. (B) Fit of two HN-functions to the dielectric loss data of exo-PNBSi at $T = 486$ K. The sold line is the whole fit function where the dashed lines represent the contributions of the individual processes

have a complete nonpolar structure, the visibility of the β-relaxation in the dielectric loss of PTCNSi1 was assigned to localized oxidized parts of the side group or the backbone. As no β-relaxation is observed for exo-PNBSi, it is be concluded that it is less oxidized, which is confirmed by FTIR.[52] At higher temperatures, a β*-process is found for PTCNSi1. This β*-process is assigned to a Maxwell/Wagner/Sillars (MWS) polarization process, due to blocking of charge carriers at internal phase boundaries. Both, PTCNSi1 and exo-PNBSi, are polymers bearing microporosity. This means, these polymers must be considered as biphasic systems consisting of a polymer and a void phase. As discussed in detail in the literature[30] the conduction mechanism in these systems is mainly a charge transport through the microporous network. During this process, charge carriers can be blocked at pore walls giving rise to a MWS polarization process. Therefore, the β*-process can be considered as immanent dielectric feature of polymers bearing intrinsic microporosity.

For this reason, the β₁*- and β₂*-processes observed for exo-PNBSi are also assigned to MWS polarization processes due to a blocking of charge carriers at the pore walls. It was shown by positron annihilation experiments that pore-size distribution of the micropores is bimodal.[53] Therefore, the appearance of two MSW polarization processes for exo-PNBSi is related to its bimodal pore-size distribution. A similar observation was made for another polynorbornene PTCNSi2g exhibiting a larger fraction of intrinsic microporosity in comparison to PTCNSi1.[30] Compared to the β₁*-, the β₂*-process of exo-PNBSi is located at lower frequencies. Therefore, it is concluded that the β₂*-process is related to the part of the bimodal pore-size distribution with larger pore sizes.
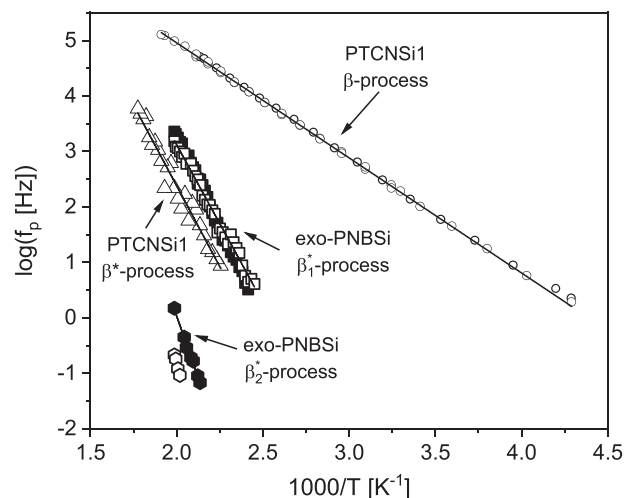

FIGURE 4 Arrhenius diagram of exo-PNBSi in comparison to PTCNSi1. exo-PNBSi: Open squares—β₁*-process, first heating; solid squares—β₁* process, second heating; open pentagons—β₂*-process, first heating; solid pentagons—β₂*-process, second heating. PTCNSi1: circles—β-relaxation; triangles—β*-process. Lines are fits of the Arrhenius equation to the data

Using standard procedures, the model function of Havriliak/Negami (HN-function) was fitted to the dielectric data. The HN-function is given by[54]

$$\varepsilon_{HN}^*(\omega) = \varepsilon_\infty + \frac{\Delta\varepsilon}{\left(1 + (i\omega\tau_{HN})^\beta\right)^\gamma}. \quad (3)$$

In Equation (3), $\Delta\varepsilon$ represents the dielectric strength, whereas the shape parameters β and γ ($0 < \beta$; $\beta\gamma \leq 1$) describe the symmetric and the asymmetric broadening of the HN- function with respect to the Debye one.[53]

The relaxation time τ_{HN} is related to the frequency of the maximal dielectric loss f_p. ε_∞ is the real part of the complex dielectric function for $\omega \rangle\rangle \tau_{HN}^{-1}$. If more than one process is observed in the available frequency window, a sum of HN-functions is fitted to the data as described in more detail elsewhere.[53] Contributions related to conductivity are treated in a conventional way by adding $\sigma_0/(\omega^s \varepsilon_0)$ to the loss part of the HN-function. The parameter σ_0 is related to the DC conductivity of the system. The exponent s models Ohmic ($s = 1$) or non-ohmic effects ($s < 1$) in the conductivity where ε_0 is the permittivity of vacuum. Figure 3B gives one example for the fitting of HN-functions to the dielectric spectra of exo-PNBSi.

From the HN-fits, the f_p values are obtained and plotted versus inverse temperature in the Arrhenius diagram (Figure 4). The rates of β_1*-process observed for exo-PNBSi are located close to that of the β*-process of PTCNSi1 but shifted slightly to lower temperatures. The rate of a MWS process can be approximately related to the inverse of an average distance of the heterogenous structure,[30] which is here related to an average pore size. It should be noted that compared to PTCNSi1 ($610 \ m^2 \ g^{-1}$), the microporosity of exo-PNBSi characterized by the BET surface is less ($540 \ m^2 \ g^{-1}$).

The temperature dependence of the rates of both processes, the β_1*- and the β_2*-process, follows the Arrhenius equation, which reads

$$f_p = f_\infty \exp\left(-\frac{E_A}{RT}\right). \tag{4}$$

Here, E_A denotes the activation energy, T is the temperature, and R is the universal gas constant. f_∞ stands for the rate at infinite temperatures. For the β_1*-process the activation energy was estimated to $108.7 \ kJ \ mol^{-1}$. This value of the activation energy is close to that of the β*-process observed for PTCNSi1, which is $111.4 \ kJ \ mol^{-1}$. The activation energy for the β_2*-process of exo-PNBSi is estimated to be $169 \ kJ \ mol^{-1}$. Moreover, compared to the β_1*-process, the β_2*-process is shifted to lower frequencies. As discussed earlier, the rate of a MWS polarization is inversely related to an average pore dimension. Therefore, the β_1*-process is related to smaller pores, whereas the β_2*-process is assigned to larger pores. A similar assignment is made in the literature.[30]

The rates of the β_1*-process are almost the same for first and second heating cycle. That means the pore structure related to the β_1*-process is most probably not changed during the thermal treatment related to the heating process. However, this is a bit different for the β_2*-process. In this case for the second heating cycle, the data are shifted to lower temperatures compared to those of

the β_1*-process. As the relaxation rate of the β_2*-process is assumed to be also related to an average pore dimension, it might be inferred that these larger pores undergo a shrinking process. This was discussed in a similar way for PTCNSi2g elsewhere.[30]

3.2 | Fast scanning calorimetry

Neither for exo-PNBSi nor for PTCNSi1 a glass transition could be observed by conventional differential scanning calorimetry before the thermal degradation of the polymers. Therefore, the thermal behavior of exo-PNBSi was investigated by fast scanning calorimetry to decouple the kinetics of the glass transition from that of thermal degradation.

Figure 5A depicts the heat flow thermograms measured for exo-PNBSi by FSC for different heating rates. They show a step-like change of the heat flow indicating a glass transition, showing the typical shift to higher temperatures for increased heating rates. The glass transition temperature T_g was estimated as the mid temperature of the step-like change of the heat flow (see Figure 5A). The thermal relaxation map is constructed by plotting the logarithm of the heating rates versus the inverse of T_g in Arrhenius coordinates in Figure 5B. Please note that the processes discussed in Figure 4 have different molecular origin. Thus, they are observed in a different temperature range than that of the dynamic glass transition. The thermal data can be well approximated by the Arrhenius law. Normally, the data for a dynamic glass transition should be curved when plotted in the relaxation map, which is not clearly reflected by the available results in this case. However, one must consider that only a quite narrow range of heating rates could be covered by FSC where an expected Vogel/Fulcher/Tammann behavior could be well approximated by an Arrhenius law. From the data, an apparent activation energy of $54.5 \ kJ \ mol^{-1}$ is estimated for exo-PNBSi.

The glass transition of PTCNSi1 is investigated by in the literature[55] also by FSC. The corresponding data are included in Figure 5B. Compared the exo-PNBSi, the glass transition temperatures estimated for PTCNSi1 show a larger scatter. The larger error of the data measured for PTCNSi1 is due to fact that the glass transition is less pronounced for this polymer compared to exo-PNBSi. This is probably due to the stiffer backbone of PTCNSi1, which restricts segmental fluctuations. The absolute values of T_g are found to be higher than that of exo-PNBSi. This can be also ascribed to the more rigid chain structure of PTCNSi1. Like for exo-PNBSi, the dependence of the inverse glass transition temperature on the heating rate can be approximated by the
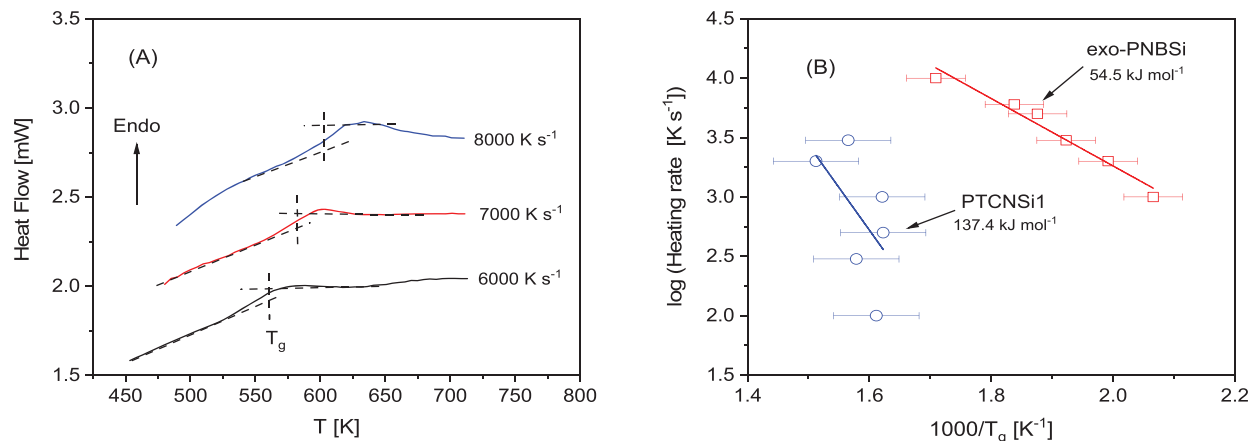
FIGURE 5 (A) FSC thermograms for exo-PNBSi for the indicated heating rates. (B) Heating rate versus inverse glass transition temperature: Red squares—exo-PNBSi: Blue circles—PTCNSi1. Line are fits of the Arrhenius equation to the data
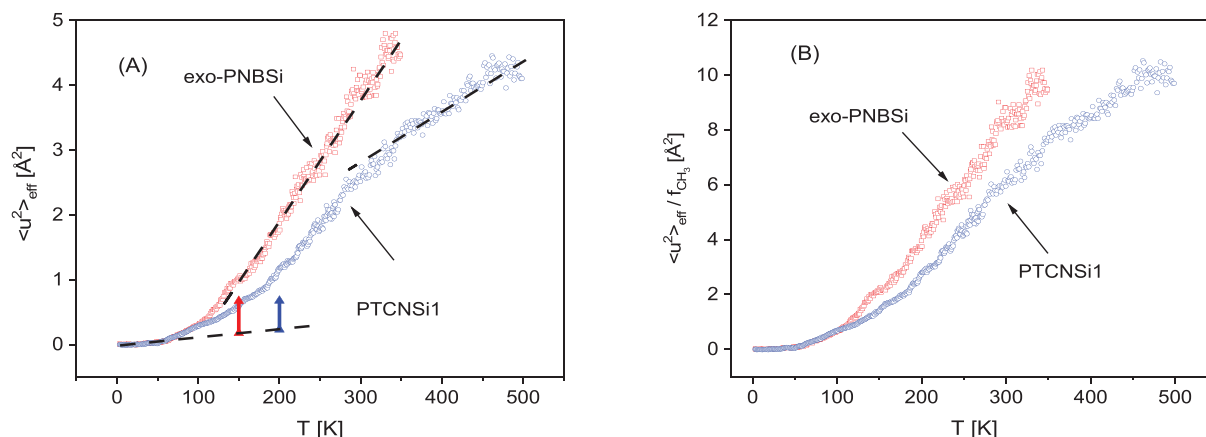

FIGURE 6 (A) Temperature dependence of the effective mean squared displacement $\langle u^2 \rangle_{eff}$: red squares—exo-PNBSi; blue circles—PTCNSi1. The dashed lines are guides for the eyes. The vertical solid lines give the theoretical contribution of the methyl groups to $\langle u^2 \rangle_{eff}$. (B) Effective mean squared displacement $\langle u^2 \rangle_{eff}$ versus temperature normalized by scattering cross sections of the methyl groups (see text): red squares—exo-PNBSi; blue circles—PTCNSi1

Arrhenius law with an apparent activation energy of 137.4 kJ mol^{-1}, which is essentially higher than the value found for exo-PNBSi. Again, this can be understood by the more rigid backbone of PTCNSi1, which is due to the cyclobutane moiety in the chemical structure.

3.3 | Neutron scattering

Quasielastic neutron scattering experiments have been reported for polymers suited for application in gas separation membranes in the literature.[20,21,26,56–58] As discussed earlier, and, for instance, in the reference 26, it was argued that molecular fluctuations at a time scales from picoseconds to nanoseconds are relevant for gas transport processes in polymeric matrices.

The temperature dependence of the effective mean squared displacement is depicted for exo-PNBSi in comparison to PTCNSi1 in Figure 6A. Vibrations are dominating the temperature dependence of the effective mean squared displacement at low temperatures up to ca. 75 K for both materials. With further increasing temperature, a step-like change is observed in the temperature dependence of $\langle u^2 \rangle_{eff}$, which indicates the onset of molecular fluctuations at a time scale which corresponds to the resolution of the backscattering spectrometer (ca. 2 ns). As molecular origin of these molecular motions one can thinks of the methyl group rotations, which are found to become activated in that temperature range.[51,59–61] As no dielectrically active relaxation process has been observed by broadband dielectric spectroscopy the molecular fluctuations must be due to nonpolar groups, which

supports the assignment of the relaxation process to the methyl group rotation.

The repeating units of both exo-PNBSi and PTCNSi1 have comparable scattering cross sections. Furthermore, both polymers have the same number on methyl groups in the unit. Therefore, without a detailed theoretical elaboration, one can conclude that the step height of effective mean squared displacement $\Delta\langle u^2\rangle_{\text{eff, CH3}}$ should be the same. Figure 6A shows that this is not the case. For a more detailed discussion, the contribution of the methyl group rotation to the effective mean squared displacement can be calculated in the long-time limit in the following way. From the geometry of the methyl group, the jump length of a hydrogen is estimated to 1.779 Å, which leads to a mean squared displacement of 1.055 Å^2. To obtain the contribution of the methyl groups to the mean squared displacement, this value has to be multiplied by the ratio of the scattering cross section for the methyl groups to the total scattering cross section f_{CH3} (see Table 1). A scaling of $\langle u^2\rangle_{\text{eff}}$ (T) by f_{CH3} should lead to a collapse of $\langle u^2\rangle_{\text{eff}}$ (T) for both polymers when the number of methyl groups is the same and the different number of hydrogen nuclei is the only difference in polymer structure (see Figure 6B). Figure 6B reveals that also this

scaling does not lead to the collapse of $\langle u^2\rangle_{\text{eff}}$ (T) measured for exo-PNBSi and PTCNSi1. Therefore, one has to conclude that the motional processes in both polymers are different. Moreover, the temperature dependencies of $\langle u^2\rangle_{\text{eff}}$ (T) for both polymers are shifted in the temperature scale. This points to a difference in the activation energy of the relaxation process for exo-PNBSi and PTCNSi1.

The theoretical values $\Delta\langle u^2\rangle_{\text{eff, CH3}}$ were included in Figure 6A as vertical double arrows. For both polymers, the theoretical contributions are smaller than the observed experimental changes, which might be an indication that in addition to the methyl group rotation, other motional processes contribute to the observed effective mean squared displacement.

Figure 7A depicts the time-dependent intermediate scattering function $S_{\text{inc}}(q,t)$ for exo-PNBSi for different q vectors at $T = 125$ K. The data up to ca. 30 ps correspond to measurements at TOFTOF, whereas the data between from ca. 60 ps to 3.2 ns are obtained from measurements at SPHERES. One step-like change is observed in $S_{\text{inc}}(q,t)$, which indicates molecular motions. Figure 7B compares $S_{\text{inc}}(q,t)$ for exo-PNBSi and PTCNSi1. At the first glance, both curves are not so much different. But a closer inspection reveals that $S_{\text{inc}}(q,t)$ measured for exo-PNBSi is shifted to slightly longer times compared to PTCNSi1. Also, the height of the plateau value in the long-time limit related to an elastic incoherent structure factor (EISF) is higher for exo-PNBSi.

It is safe to assume that the methyl group rotation will at least contribute to the relaxation process observed by neutron scattering. As discussed in the literature, the rotation rate distribution model (RRDM)[51] is considered as a kind of standard model for the methyl group
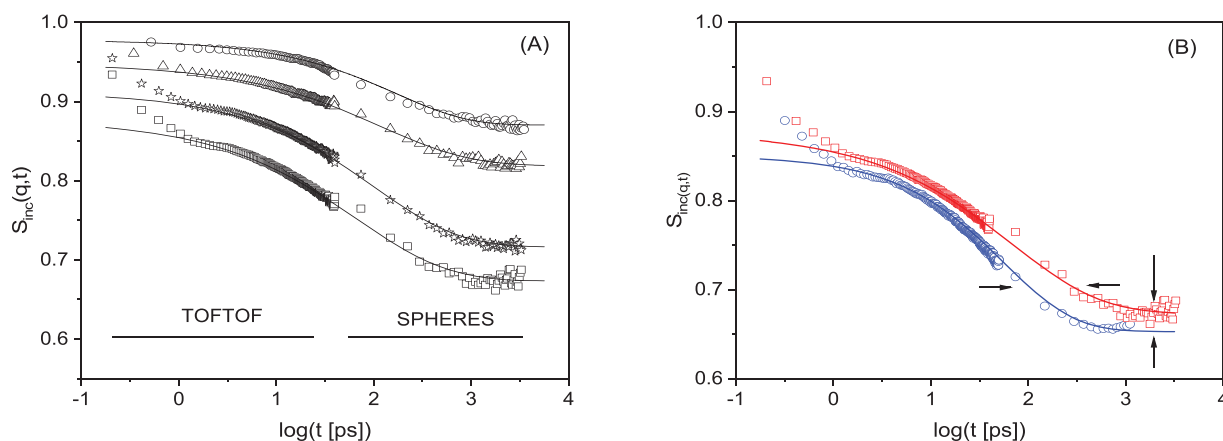
TABLE 1 Relative scattering cross section of the methyl group f_{CH3} and contribution of the methyl groups to the effective mean squared displacement $\Delta\langle u^2\rangle_{\text{eff, CH3}}$,

	exo-PNBSi	PTCNSi1
f_{CH3}	0.471	0.423
$\Delta\langle u^2\rangle_{\text{eff, CH3}}$	0.497 Å^2	0.446 Å^2

FIGURE 7 (A) $S_{\text{inc}}(q,t)$ measured for exo-PNBSi at $T = 125$ K: circles—$q = 0.693$ Å^{-1}, triangles—$q = 1.039$ Å^{-1}, asterisks—$q = 1.417$ Å^{-1}, squares—$q = 1.761$ Å^{-1}. Lines are fits of Equation (5) to the corresponding data. (B) $S_{\text{inc}}(q,t)$ measured at $T = 125$ K: red squares—exo-PNBSi, $q = 1.761$ Å^{-1}; blue circles—PTCNSi1, $q = 1.78$ Å^{-1}. Lines are fits of Equation (5) to the corresponding data. The arrows point to the observed differences
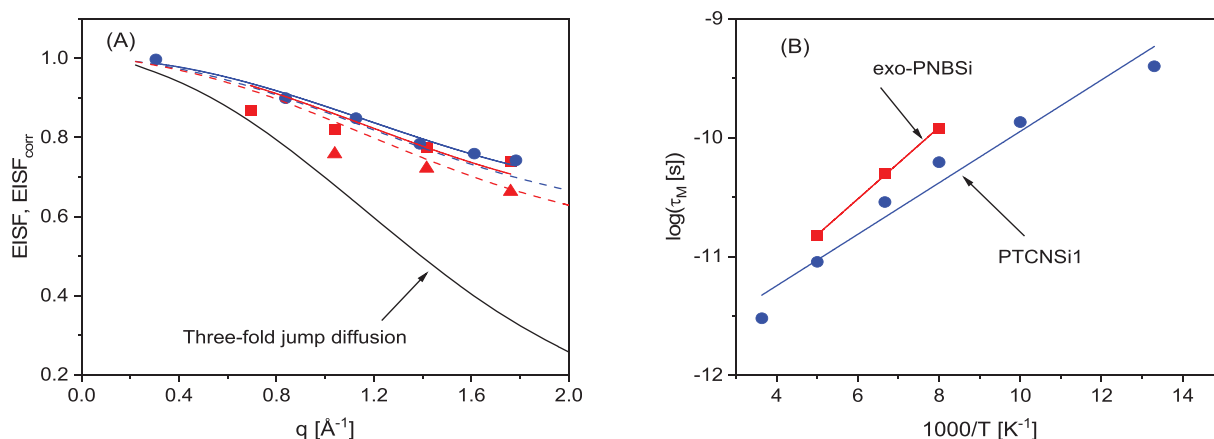
FIGURE 8 (A) q-dependence of the EISF: red squares—data for exo-PNBSi at $T = 150$ K, red triangles—data for exo-PNBSi at $T = 200$ K. Dashed red line—calculated by Equation (7) with the theoretical value of $C_{fix} = 0.5$ to $T = 150$ K. Solid red line fit of Equation (7) leading to $C_{fix} = 0.5603$. Blue circles data for PTCNSi1 at $T = 150$ K. Data for PTCNSi1 were taken from the literature.[31]. Dashed blue line —calculated by Equation (7) with the theoretical value of $C_{fix} = 0.55$ at $T = 150$ K. Solid blue line fit of Equation (7) leading to $C_{fix} = 0.52$. The black line is the prediction of the threefold jump diffusion model as calculated by Equation (6). (B) Relaxation time τ_M versus inverse temperature: red squares—exo-PNBSi. Blue circles—PTCNSi1. Data for PTCNSi1 were taken from the literature.[31] Lines are fits of the Arrhenius equation to the corresponding data

rotation. Here, a simplified approach is employed by fitting a stretched exponential function to the data. In detail, the fit function reads

$$S_{inc}(q,t) = \text{DWF} * \left((1 - \text{EISF}) \exp\left(-\left(\frac{t}{\tau_M} \right)^{\beta_M} \right) + \text{EISF} \right). \tag{5}$$

The parameters have the following meanings: DWF is the Debye/Waller factor, τ_M is the relaxation time, β_M is the stretching parameter, and EISF is the elastic incoherent structure factor. As indicated by Figure 7A, the data can be well described by that approach.

In the jump diffusional model for the methyl rotation, a threefold potential $V(\phi) \sim (1 - \cos(3\phi))/2$ is employed, which results in three equivalent energy minima with respect to the rotation angle ϕ of the methyl group. In the framework of this model, the EISF for the methyl group rotation can be calculated to

$$\text{EISF}(q) = \frac{1}{3}\left(1 + 2\frac{\sin(\sqrt{3}qr)}{\sqrt{3}qr} \right). \tag{6}$$

The radius of a circle spanned by the positions of the hydrogen nuclei of the methyl group is $r = 1.027$ Å.[51]

Figure 8A gives the q dependence of estimated EISF for PTCNSi1 for $T = 150$ K. Clearly the experimental data cannot be described by the q-dependence predicted by Equation (6). To discuss this issue further one has to

consider that not all hydrogen nuclei of the repeating unit are located in the methyl group. The repeating unit of PTCNSi1 has 20 hydrogen nuclei of which 9 protons are participating in the methyl group rotation. This means 11 hydrogen nuclei scatter elastically. Therefore, Equation (6) has to be modified with respect to the fraction C_{fix} of hydrogen nuclei, which scatter elastically[21,51,59–62]:

$$\text{EISF}_{corr}(q) = (1 - C_{fix})\text{EISF}(q) + C_{fix}. \tag{7}$$

As shown by Figure 8A, this approach describes the data for PTCNSi1 reasonably well even with the theoretical fraction $C_{fix} = 0.55$ deduced from the chemical structure of the repeating unit. A fit of Equation (7) leads to a value of C_{fix} of 0.52, which is close to the theoretical one.

The situation is a bit different for exo-PNBSi. In this case, the data can be only poorly described with Equation (7) with the theoretical fraction of C_{fix} of 0.5 (see Figure 8A). Also, a fit of Equation (7) does not lead to an improvement. The q-dependence of the EISF predicted by Equation (7) seems to be different from that which is observed experimentally. Therefore, one has to conclude that in addition to methyl group rotation, further motional processes do contribute to the observed relaxation. This conclusion agrees with the temperature dependence of the effective mean squared displacement, which shows an increased dynamics compared to the theoretical prediction from the methyl group rotation (see Figure 6A). Colmenero and Arbe provided some experimental evidence for a fast dynamical process between

100 and 200 K, which was assigned to the carbon–carbon torsional barrier.[63] Such fluctuations seem to be possible for both polymer backbones. Therefore, the increased dynamics observed in the temperature dependence of $\langle u^2 \rangle_{\text{eff}}$ for both polymers and in $S_{\text{inc}}(q,t)$ for exo-PNBSi may be assigned to such carbon–carbon torsional barrier fluctuations. However, the cyclobutane ring, present in the repeating unit of PTCNSi1, will hinder such carbon–carbon torsional fluctuation more than the more flexible chain structure of exo-PNBSi. Therefore, the observed values of the effective mean squared displacement of exo-PNBSi are higher than those of PTCNSi1. In the literature,[62] the carbon–carbon torsional fluctuation was also related to the glass transition. Therefore, the lower values of $\langle u^2 \rangle_{\text{eff}}$ observed for PTCNSi1 are in agreement with the higher glass transition temperature observed for that polymer.

Finally, the temperature dependence of the relaxation time τ is considered. As expected for localized fluctuations the relaxation time is found to be independent of the q vector. The relaxation time τ is plotted versus inverse temperature in Figure 8B. The data for both polymers can be described by the Arrhenius equation. The activation energy is estimated to 5.8 kJ mol^{-1} for exo-PNBSi, which is higher value of 4.2 kJ mol^{-1} for PTCNSi1.

To conclude the neutron scattering experiments, it should be noted that these investigations are motivated by the idea that especially localized molecular fluctuations can play the role door openers of bottlenecks between pores to allow for the diffusion of gasses.

4 | CONCLUSION

Polymers bearing intrinsic microporosity are considered as promising materials for the active separation layer in separation membranes. Generally, the diffusion of small penetrant molecules in condensed polymer materials is related to the molecular mobility of these materials. Polymers with intrinsic microporosity exhibit very high permeabilities due to the existence of a continuous network of micropores, which is favorable for gas separation. What makes them even more promising for this application is their reasonable permselectivity, which is only poorly understood in this context. As such a selectivity is usually ascribed to a thermally activated size discriminating process, it is discussed that for microporous polymers this is also related to molecular fluctuations, which can dynamically open and close bottlenecks between micropores. Therefore, it is essential to investigate the molecular mobility in these

materials to better understand the gas transport and to optimize these membrane polymers.

Here, the molecular mobility of two high-performance polynorbornenes, exo-PNBSi and PTCNSi1, was investigated by a combination of broadband dielectric spectroscopy, fast scanning calorimetry, and quasielastic neutron scattering. Both polymers were prepared by addition polymerization. They have different backbone structures but similar trimethylsilyl side groups.

In the dielectric spectra of PTCNSi1, two relaxation processes are described in the literature. The process at lower temperatures or higher frequencies is assigned to localized fluctuation of oxidized parts of the main chain or the side groups. The second process found at higher temperatures or corresponding lower frequencies is related to a MWS-polarization process due to the blocking of charge carriers at micropore walls. For exo-PNBSi, two dielectrically active processes are found, which are both assigned to MWS-polarizations. The fact that two MWS processes are observed for exo-PNBSi points to a bimodal size distribution of the micropores in comparison to PTCNSi1, which is supported by positron annihilation experiments reported in the literature.[53]

By employing fast scanning calorimetry, a glass transition could be evidenced for both polymers, which was not observable by conventional DSC due to thermal degradation. The glass transition temperature is found to be higher for PTCNSi1 compared to exo-PNBSi. Also, the apparent activation energy for glass dynamics is higher for PTCNSi1. Both results are discussed considering the more rigid backbone structure of PTCNSi1 due to the cyclobutane ring, which is not present in the chain structure of exo-PNBSi.

The molecular dynamics on microscopic time and length scales was further investigated by quasielastic neutron scattering. Fixed elastic windows scans show the onset of molecular motion at a time scale of ca. 2 ns at approximately 75 K for both polymers. As molecular origin for the fluctuations, one can consider the methyl group rotations. However, the calculated theoretical contributions for the methyl group rotations are much smaller than the observed experimental changes. Therefore, it must be concluded that other motional processes might also contribute to the experimentally observed mean squared displacement. The quasielastic spectra show one relaxation process. Form the q-dependence of the observed EISF, it was concluded that for PTCNSi1 the observed relaxation process is mainly due to the methyl group rotation. This is different for exo-PNBSi where the observed q-dependence for the EISF does not follow the expected behavior for the methyl group

rotation. It was concluded that observed relaxation process is partly due to the methyl group rotation, which is overlaid by a further process. Here, one can think of carbon–carbon torsional fluctuations of the backbone. Such fluctuations seem to be possible for both polymers although its influence seems to be stronger for exo-PNBSi compared to PTCNSi1 due to the less stiff backbone of the former polymer.

In further work, the obtained results will be compared with data for other polymers bearing an intrinsic microporosity like PIMs.

ACKNOWLEDGMENTS

DATA AVAILABILITY STATEMENT
The data are part of an ongoing reserach project.

REFERENCES

[1] J. G. Wijmans, R. W. Baker, _J. Membr. Sci._ **1995**, _107_, 1.

[2] W. J. Koros, B. J. Story, S. M. Jordan, K. O'Brien, G. R. Husk, _Polym. Eng. Sci._ **1987**, _27_, 603.

[3] J. H. Petropoulos, in _Polymeric Gas Separation Membranes_ (Eds: D. R. Paul, Y. P. Yampolskii), CRC Press, Boca Raton **1994**.

[4] M. Böhning, N. Hao, A. Schönhals, _J. Polym. Sci. Polym. Phys._ **2013**, _51_, 1593.

[5] R. W. Baker, _Membrane Technology and Applications_, John Wiley & Sons, Chichester, UK **2004**.

[6] Y. Yampolskii, _Macromolecules_ **2012**, _45_, 3298.

[7] L. M. Robeson, _J. Membr. Sci._ **2008**, _320_, 390.

[8] M. Mohammadi, S. Shirazian, M. Asaollahzade, L. Jamshidy, A. Hemmati, _Polym. Eng. Sci._ **2015**, _55_, 975.

[9] T. Higashimura, T. Masuda, M. Okada, _Polym. Bull._ **1983**, _10_, 114.

[10] T. Masuda, M. Kawasaki, Y. Okano, T. Higashimura, _Polym. J._ **1982**, _14_, 371.

[11] A. Morisato, I. Pinnau, _J. Membr. Sci._ **1996**, _121_, 243.

[12] Y. Hu, M. Shiotsuki, F. Sanda, B. D. Freeman, T. Masuda, _Macromolecules_ **2008**, _41_, 8525.

[13] P. M. Budd, K. J. Msayib, C. E. Tattershall, B. S. Ghanem, K. J. Reynolds, N. B. McKeown, D. Fritsch, _J. Membr. Sci._ **2005**, _251_, 263.

[14] M. Carta, R. Malpass-Evans, M. Croad, Y. Rogan, J. C. Jansen, P. Bernardo, F. Bazzarelli, N. B. McKeown, _Science_ **2013**, _339_, 303.

[15] Y. P. Yampolskii, _Polym. Rev._ **2017**, _57_, 200.

[16] P. P. Chapala, M. V. Bermeshev, L. E. Starannikova, N. A. Belov, V. E. Ryzhikh, V. P. Shantarovich, V. G. Lakhin, N. N. Gavrilova, Y. P. Yampolskii, E. S. Finkelshtein, _Macromolecules_ **2015**, _48_, 8055.

[17] M. Gringolts, M. Bermeshev, Y. Yampolskii, L. Starannikova, V. Shantarovich, E. Finkelstein, _Macromolecules_ **2010**, _43_, 7165.

[18] D. A. Alentiev, M. Bermeshev, _Polym. Rev._ **2021**, _38_, 1.

[19] X. Wang, T. J. Wilson, D. Alentiev, M. Gringolts, E. Finkelshtein, M. Bermeshev, B. K. Long, _Polym. Chem._ **2021**, _12_, 2947.

[20] R. Zorn, P. Szymoniak, M. A. Kolmangadi, M. Wolf, D. Alentiev, M. Bermeshev, M. Böhning, A. Schönhals, _Phys. Chem. Chem. Phys._ **2020**, _22_, 18381.

[21] R. Zorn, P. Szymoniak, M. A. Kolmangadi, R. Malpass-Evans, N. B. McKeown, M. Tyagi, M. Böhning, A. Schönhals, _Crystals_ **2021**, _11_, 1482.

[22] D. Hofmann, M. Heuchel, Y. Yampolskii, V. Khotimskii, V. Shantarovich, _Macromolecules_ **2002**, _35_, 2129.

[23] M. Heuchel, D. Fritsch, P. M. Budd, N. B. McKeown, D. Hofmann, _J. Membr. Sci._ **2008**, _318_, 84.

[24] W. J. Koros, C. Zhang, _Nat. Mater._ **2017**, _16_, 289.

[25] A. Fuoco, C. Rizzuto, E. Tocci, M. Monteleone, E. Esposito, P. M. Budd, M. Carta, B. Comesañ-Gándara, N. B. McKeown, J. C. Jansen, _J. Mater. Chem. A_ **2019**, _7_, 20121.

[26] R. Inoue, T. Kanaya, T. Masuda, K. Nishida, O. Yamamuro, _Macromolecules_ **2012**, _45_, 6008.

[27] M. A. Kolmangadi, P. Szymoniak, G. J. Smales, M. Bermeshev, A. Schönhals, M. Böhning, _J. Membr. Sci. Res._ **2022**, _8_, 538060 https://doi.org/10.22079/JMSR.2021.538060.1495

[28] D. A. Alentiev, M. V. Bermeshev, L. E. Starannikova, E. V. Bermesheva, V. P. Shantarovich, V. G. Bekeshev, Y. P. Yampolskii, E. S. Finkelshtein, _J. Polym. Sci., Part A: Polym. Chem._ **2018**, _56_, 1234.

[29] M. Mazo, M. Balabaev, A. Alentiev, Y. Yampolskii, _Macomolecules_ **2018**, _51_, 1398.

[30] H. Yin, P. Chapala, M. Bermeshev, B. R. Pauw, A. Schönhals, M. Böhning, _ACS Appl. Polym. Mater._ **2019**, _1_, 844.

[31] A. Schönhals, P. Szymoniak, M. A. Kolmangadi, M. Böhning, M. Zamponi, B. Frick, M. Appel, G. Günther, M. Russina, D. A. Alentiev, M. Bermeshev, R. Zorn, _J. Membr. Sci._ **2022**, _642_, 119972.

[32] N. Yevlampieva, M. Bermeshev, A. Gubarev, P. Chapla, M. Antipov, _Polym. Sci. Ser. A_ **2016**, _58_, 324.

[33] G. Strobl, _The Physics of Polymers: Concepts for Understanding Their Structures and Behavior_, Springer, Berlin, Heidelberg, **2007**.

[34] F. Kremer, A. Schönhals, in _Broadband Dielectric Spectroscopy_ (Eds: F. Kremer, A. Schönhals), Springer, Berlin, Heidelberg, **2003**, p. 35.

[35] V. Mathot, M. Pyda, T. Pijpers, G. V. Poel, E. van de Kerkhof, S. van Herwaarden, F. van Herwaarden, A. Leenaers, _Thermochim. Acta_ **2011**, _522_, 36.

[36] https://www.wacker.com/h/en-us/silicone-fluids-emulsions/linear-silicone-fluids/wacker-ak-60000/p/000023055

[37] P. Cebe, X. Hu, D. L. Kaplan, E. Zhuralev, A. Wurm, D. Arbeiter, C. Schick, _Sci. Rep._ **2013**, _3_, 1130.

[38] P. Cebe, B. P. Partlow, D. L. Kaplan, A. Wurm, E. Zhuralev, C. Schick, _Thermochim. Acta_ **2015**, _615_, 8.

[39] H. Yin, Y. Chua, B. Yang, C. Schick, W. Harrison, P. M. Budd, M. Böhning, A. Schönhals, _J. Phys. Chem. Lett._ **2018**, _9_, 2003.

[40] H. Yin, B. Yang, Y. Z. Chua, P. Szymoniak, M. Carta, R. Malpass-Evans, N. McKeown, W. J. Harrison, P. M. Budd, C. Schick, M. Böhning, A. Schönhals, *ACS Macro Lett.* **2019**, *8*, 1022.

[41] M. Kolmangadi, P. Szymoniak, G. J. Smales, D. Alentiev, M. Bermeshev, M. Böhning, A. Schönhals, *Macromolecules* **2020**, *53*, 7410.

[42] D. Thomas, C. Schick, P. Cebe, P., *Thermochim. Acta* **2018**, *667*, 65.

[43] N. Cano Murillo, P. Szymoniak, G. J. Smales, H. Sturm, A. Schönhals, *ACS Appl. Polym.* **2021**, *3*, 6572.

[44] M. Bée, *Quasielastic Neutron Scattering, Principles and Applications in Solid State Chemistry, Biology and Materials Science*, Adam Hilger, Bristol, UK **1988**.

[45] H. M.-L. Zentrum, *J. Large-Scale Res. Facil.* **2015**, *1*, A30. https://doi.org/10.17815/jlsrf-1-38

[46] J. Wuttke, A. Budwig, M. Drochner, H. Kämmerling, F.-J. Kayser, H. Kleines, V. Ossovyl, L.-C. Pardo, M. Prager, D. Richter, G. J. Schneider, H. Schneider, S. Staringer, *Rev. Sci. Instrum* **2012**, *83*, 075109.

[47] R. Zorn, *Nucl. Instrum. Methods Phys. Res.* **2009**, *603*, 439.

[48] TOFTOF, *J. Large-Scale Res. Facil* **2015**, *1*, A15. https://doi.org/10.17815/jlsrf-1-40

[49] F. Rieutord, *INX-Program for Time-of-Flight Data Reduction*, ILL Internal Publication, Grenoble, 90RI17T, **1990**.

[50] O. G. Randl, *SQW - A comprehensive user manual*, ILL Internal Publication, Grenoble, 96RA07T, **1996**.

[51] R. Zorn, B. Frick, L. Fetters, *J. Chem. Phys.* **2002**, *116*, 845.

[52] M. A. Kolmangadi, *Dielectric and calorimetric properties of super glassy polynorbornene films*, Master thesis, Technische Universität, Berlin, **2020**.

[53] E. S. Finkelshtein, K. Makovetskii, M. Gringolts, Y. V. Rogan, T. Golenko, L. Starannikova, Y. P. Yamploskii, V. Shantarovich, T. Suzuki, *Macromolecules* **2006**, *39*, 7022.

[54] A. Schönhals, F. Kremer, in *Broadband Dielectric Spectroscopy* (Eds: F. Kremer, A. Schönhals), Springer, Berlin **2003**, p. 59.

[55] P. Szymoniak, M. A. Kolmangadi, A. Schönhals, et al., *Appl. Sci.* **2022**. Unpublished.

[56] T. Kanaya, M. Teraguchi, T. Masuda, K. Kaji, *Polymer* **1999**, *40*, 7157.

[57] T. Kanaya, I. Tsukushi, K. Kaji, T. Sakaguchi, G. Kwak, T. Masuda, *Macromolecules* **2002**, *35*, 5559.

[58] R. Zorn, W. Lohstroh, M. Zamponi, W. J. Harrison, P. M. Budd, M. Böhning, A. Schönhals, *Macromolecules* **2020**, *53*, 6731.

[59] J. Colmenero, A. Moreno, A. Alegria, *Prog. Polym. Sci.* **2005**, *30*, 1147.

[60] A. Schönhals, C. Schick, H. Huth, B. Frick, M. Mayorova, R. Zorn, *J. Non-Cryst. Solids* **2007**, *353*, 3853.

[61] A. Schönhals, R. Zorn, B. Frick, *Polymer* **2016**, *105*, 393.

[62] A. Yildirim, C. Krause, R. Zorn, W. Lohstroh, M. Zamponi, O. Holderer, B. Frick, A. Schönhals, *Soft Matter* **2020**, *16*, 2005.

[63] J. Colmenero, A. Arbe, *Phys. Rev. B* **1998**, *57*, 1358.